RSC Advances

PAPER

View Article Online
View Journal | View Issue

Check for updates

Cite this: *RSC Adv.*, 2020, **10**, 15320

Experimental study on the kinetic effect of *N*-butyl-*N*-methylpyrrolidinium tetrafluoroborate and poly(*N*-vinyl-caprolactam) on CH_4 hydrate formation

Jun-Jie Ren,[abcd] Zhi-Lin Lu,[abce] Zhen Long *[abc] and Deqing Liang [abc]

In this work, a series of experiments were carried out to study the kinetic inhibition performance of *N*-butyl-*N*-methylpyrrolidinium tetrafluoroborate ([BMP][BF_4]), poly(*N*-vinylcaprolactam) (PVCap) and compound inhibitor systems on methane hydrate from both macroscopic and microscopic perspectives. In the macroscopic experiments, the influence of the concentration, the ratio of inhibitors, the subcooling on the induction time and gas consumption rate of methane hydrate were studied. The results indicated that [BMP][BF_4] could inhibit the growth rate of CH_4 hydrate, but failed to delay the nucleation. An improved inhibitory effect was observed by combining [BMP][BF_4] and PVCap, and the optimal ratio of the two inhibitors was obtained to gain the best inhibition performance. Furthermore, the microstructure and morphology of methane hydrate crystals formed in different inhibitor systems were investigated through powder X-ray diffraction (PXRD), Raman spectroscopy and scanning electron cryomicroscopy (Cryo-SEM) methods. It was found that [BMP][BF_4] and PVCap had different influences on the large cage occupancy by CH_4 and the morphology of methane hydrate.

Received 29th December 2019
Accepted 31st March 2020

DOI: 10.1039/c9ra10998f

rsc.li/rsc-advances

Open Access Article. Published on 17 April 2020. Downloaded on 7/25/2025 1:18:10 AM.
This article is licensed under a Creative Commons Attribution-NonCommercial 3.0 Unported Licence.

1. Introduction

Gas hydrate, also referred to as clathrate hydrate, is an ice-like solid in which the gas molecules (guest) are trapped in different-size polyhedral cavities composed of hydrogen-bonded water molecules (host).[1] Components of natural gases, such as methane, ethane, propane, and carbon dioxide, could form gas hydrates under relatively low temperature and high pressure. There are three common hydrate structures, namely cubic structure I (sI), cubic structure II (sII) and hexagonal structure H (sH), differing from each other in the size of the guest molecules and the shape of the hydrate cages.[2,3] Despite the worldwide discovery of the abundance of naturally occurring gas hydrates as potential energy, gas hydrates have been regarded as a hazard in the oil and gas industry since the 1930s, because the formation of gas hydrate gives rise to serious engineering accidents, huge economic losses and ecological risks.[4–6]

Many methods have been adopted to prevent the formation of gas hydrate, among which injecting chemicals such as thermodynamic hydrate inhibitors (THIs) and low dosage hydrate inhibitors (LDHIs) is the most common methods.[7] Methanol or glycol, representative as traditional THIs, can shift the hydrate equilibrium phase boundary to a lower temperature and higher pressure, which is unfavourable for hydrate formation.[8,9] However, great amount of THIs are needed to be effective (up to 50 vol%), which can cost a lot for post processing and be a burden to the environment.[8,10,11] LDHIs, consisting of kinetic hydrate inhibitors (KHIs) and anti-agglomerates (AAs), are effective at low concentrations (usually less than 1.0 wt%). KHIs retard the formation kinetics of hydrate crystals by prolonging the nucleation time and/or slowing down the growth rate of crystals.[12] In contrast, AAs allow hydrate to form, but keep the particles small and well dispersed in the hydrocarbon liquid.[13,14] Kinetic inhibitors usually are some water soluble polymers, such as poly(*N*-vinylpyrrolidone) (PVP) and poly(*N*-vinyl-caprolactam) (PVCap). These chemicals are often used as standards to compare the performance of other inhibitors.[15–20] However, KHIs are strictly limited by low subcooling (usually less than 10 K) and lose their effectiveness when the ultra-low temperature is encountered.[1,5] It was found that the performance of KHIs could be efficiently boosted when some chemicals were used in conjunction with KHIs.[21–24] Such chemicals

[a]*CAS Key Laboratory of Gas Hydrate, Guangzhou Institute of Energy Conversion, Chinese Academy of Sciences, Guangzhou 510640, China. E-mail: longzhen@ms.giec.ac.cn*

[b]*Guangdong Provincial Key Laboratory of New and Renewable Energy Research and Development, Guangzhou, Guangdong 510640, China*

[c]*Guangzhou Center for Gas Hydrate Research, Guangzhou Institute of Energy Conversion, Chinese Academy of Sciences, Guangzhou 510640, China*

[d]*University of Chinese Academy of Sciences, Beijing 100049, China*

[e]*Nano Science and Technology Institute, University of Science and Technology of China, Suzhou, Jiangsu 215123, China*

This journal is © The Royal Society of Chemistry 2020

Open Access Article. Published on 17 April 2020. Downloaded on 7/25/2025 1:18:10 AM.
This article is licensed under a Creative Commons Attribution-NonCommercial 3.0 Unported Licence.

are called synergists, which are effective and of great value. However, they have not got corresponding attention.[21] Ionic liquids (ILs), a kind of liquid salts at room temperature, comprise bulky and asymmetric organic cations and organic or inorganic anions. Most of them are thermally stable, non-flammable, non-toxic and environmentally friendly. They can be designed into a specific structure deliberately to achieve the applications in various fields.[25,26,27] Considering the aforementioned properties of ionic liquids, they may have the potential to be thermodynamic inhibitors. Xiao *et al.*[25] first reported that five imidazolium-based ILs (dual function inhibitors) could not only act as THIs, but also as KHIs on the formation of gas hydrate. Xiao *et al.* reported that the inhibitory effect of ILs depended on the anions and the length of alkyl chain substituents of the cations.[28] Behzad Partoon *et al.*[29] experimentally studied the performances of [EMIM][Cl] and [OH-EMIM][Cl] as LDHIs and found that [EMIM][Cl] could act as synergist in the presence of monoethylene glycol (MEG) at pressures above 35.3 MPa. In addition, Xiao *et al.* found that tetrafluoroborate ILs performed better than other ILs due to their stronger hydrogen bond, and they were much better than poly(*N*-vinylpyrrolidone) (PVP), which was generally considered to be an effective KHI. Shen *et al.*[30] investigated several kinds of ILs on the formation of methane hydrate and found that the inhibition performance of [BMP][BF_4] was better than PVP at the same concentration. Lee *et al.*[31–33] found that adding ILs to the PVCap system could enhance the inhibition effect on the hydrate formation.

Amounts of data on the thermodynamic inhibitory effect of ILs have been revealed.[34] However, there are limited researches on the kinetic synergetic effect of ILs in the presence of KHIs, especially from the microscopic level. In this work, the kinetic synergetic effect of *N*-butyl-*N*-methylpyrrolidinium tetrafluoroborate ([BMP][BF_4]) on the formation of methane hydrate in the presence of poly(*N*-vinylcaprolactam) (PVCap) was studied. The chemical structures of [BMP][BF_4] and PVCap are drawn in Fig. 1. The nucleation rate and the growth rate of methane hydrate were represented by the induction time and the gas consumption rates, respectively. These two parameters could be used to evaluate the inhibitory performance. The powder X-ray diffraction (PXRD), Raman spectroscopy (Raman) and scanning electron microscopy (SEM) were used to investigated the inhibitory effects of the inhibitors from a microscopic viewpoint and the related inhibition mechanism was proposed.

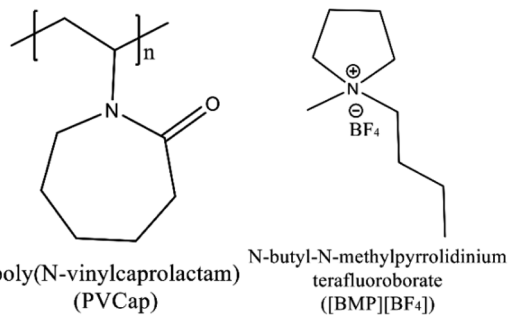

Fig. 1 Chemical structure of [BMP][BF_4] and PVCap.

2. Experimental methods

2.1 Experimental materials

The chemicals used in the experiments are listed in Table 1. The ionic liquid [BMP][BF_4] was purchased from Lanzhou Institute of Chemical Physics with a purity of 0.99 mass fraction. PVCap was synthesized in the laboratory and the gel permeation chromatography (GPC) indicated that the number average molecular weight (M_n) was 10 522 g mol^{-1} and weight average molecular weight (M_w) was 15 275 g mol^{-1}, which indicated the polydispersity index (PDI) was 1.36. Deionized water was made in the laboratory and used to prepare solutions. The mass of the materials was weighed using an electronic analytical balance with an uncertainty of $\pm$0.1 mg.

2.2 Apparatus and procedures

2.2.1 Apparatus and procedures for macroscopic experiments. Macroscopic experiments were performed on a kinetic experimental platform, the schematic diagram is drawn in Fig. 2. The stainless-steel reactor with an internal volume of 100 mL could withstand a pressure of 20 MPa and was immersed in a water bath that controlled the temperature. A magnetic stirrer and a stirring seed were used to agitate the aqueous solutions. A gas buffer cell with a volume of 156.5 mL was used to precool and store the experimental gas. A platinum resistance thermometer (PT100) with an accuracy of $\pm$0.1 K and a pressure transducer (CYB-20S) ranging from 0 to 20 MPa with an uncertainty of $\pm$0.025 MPa were used to measure the internal temperature and pressure of the reactor, respectively. The experimental data were collected by an Agilent Data Logger and recorded in an EXCEL form at an interval of 10 s.

The macroscopic experimental procedure was as follows. First, the cell was thoroughly washed with deionized water and the experimental aqueous solution three times. Then 30 mL of the experimental aqueous solution or pure water were added into the cell. Secondly, the thermostatic water bath was turned on to adjust the temperature to the set value. During this time, the magnetic stirrer was turned on to enhance heat transfer. Then the system was evacuated by a vacuum pump for about 5 min and washed with methane gas three times. When the temperature was stable, the magnetic stirrer was turned off and then methane gas was introduced into the system from the gas buffer cell until the desired pressure was reached. Finally, when the pressure and temperature were both reached and stabilized at the set value, the magnetic stirrer was turned on at a rate of 800 rpm and the recording of experimental data was commenced.

Induction time was usually defined as a period range from the time that the system reached hydrate equilibrium conditions to the formation of hydrate nucleus of critical size.[35] In this work, it was defined as the period from the start of the agitation after the experimental conditions were stable to the moment at which catastrophic hydrate was formed and was remarked by an abrupt pressure drop accompanied with a sharp increase of the temperature. Due to the stochastic hydrate nucleation, each run was repeated for at least three times with

Open Access Article. Published on 17 April 2020. Downloaded on 7/25/2025 1:18:10 AM.
This article is licensed under a Creative Commons Attribution-NonCommercial 3.0 Unported Licence.

Table 1 List of the materials used for the experiments

Chemicals	Abbreviation	Molecular weight (g mol^{-1})	Purity (%)	Supplier
N-Butyl-*N*-methylpyrrolidinium tetrafluoroborate	[BMP][BF_4]	229.07	≥99	Lanzhou Institute of Chemical Physics
Poly(*N*-vinylpyrrolidone) K90	PVP K90	360 000	—	Tokyo Chemical Industry Co., Ltd
Poly(*N*-vinylcaprolactam)	PVCap	15 275	—	Laboratory-made
Methane gas	CH_4	16	99.99	Foshan Kodi Gas Chemical Industry Co., Ltd.
Deionized water	H_2O	18	—	Laboratory-made

fresh inhibitor aqueous solution. A statistical method was used to obtain the averaged induction time and error. The consumption rate of methane gas was also analysed by the collected experimental data. In an isochoric reactor, the moles of consumed methane gas could be calculated with the change of the pressure and the temperature of the gas. For all the macroscopic experimental runs, the cumulative moles of consumed CH_4 at time t were calculated from the following equation:

$$n = \frac{P_0 V}{Z_0 R T_0} - \frac{P_t V}{Z_t R T_t} \quad (1)$$

where P_t and T_t are the pressure and temperature at time t; P_0 and T_0 are the initial values; V is the volume of the gas phase in the reactor and considered to be a constant 70 mL, R is the universal gas constant. The compressibility factor Z is calculated from an improved Peng–Robinson equation of state.[36,37]

2.2.2 Apparatus and procedures for microscopic experiments. The microscopic experiments were conducted with the powder X-ray diffraction (PXRD), Raman spectrometer and scanning electron cryomicroscopy (Cryo-SEM) measurements. All the samples were prepared at 6.95 MPa and 275.15 K, and temporarily stored in liquid nitrogen to avoid decomposition.

PXRD (X'Pert Pro MPD, PANalytical) was used to determine the type of hydrate crystal. The instrument was performed by using Cu Kα radiation ($\lambda = 1.5406$ Å) and parallel beam optics in the $\theta/2\theta$ step scan mode. The scanning range was 5–80° and the scanning step width was 0.017°. About 0.5 g of hydrate sample was fully grounded into a fine powder under liquid nitrogen, and transferred to the precooled sample table quickly. The sample was pressed and smoothed with a flat spade, and was covered quickly. The experimental temperature was kept constant at 183.15 K during the experiment.

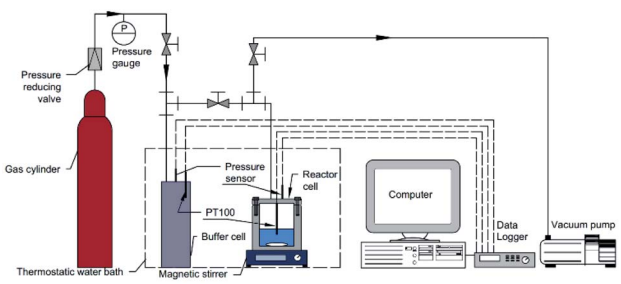

Fig. 2 Schematic diagram of experimental apparatus.

Raman spectra were collected by a confocal Raman spectrometer (LabRAM HR800, Horiba) equipped with a high-performance CCD detector and Olympus microscope. An Ar^+ laser emitting a wavelength of 532 nm was used as the excitation source at a maximum output power of 50 mW. In this work, the device temperature was operated at 183.15 K with an ambient pressure N_2 atmosphere. Hydrate samples for Raman analyses were prepared in the same way as those for PXRD analyses. After they were loaded into a quartz crucible which was placed in a cooling and heating stage (Linkam BCS), the laser was focused on their surface. The spectra were detected at regular time intervals. Structure and cage occupation information of hydrate samples can be determined by Raman spectrum analysis.[38,39]

Cryo-SEM (S-4800, Hitachi) could provide high-precision microscopic surface morphology information of hydrate samples formed in different systems. A small amount of gas hydrate samples were wrapped in tin foil on the sample holder. The prepared hydrate samples were then loaded on the SEM sample chamber *via* a refrigerated delivery system. The hydrate samples were observed and photographed at 100 K. It is worth noting that a built-in metal cutter was used to cut or crack the surface of the hydrate sample in the pre-treatment room of the freezing transmission system in order to expose the fresh and clean parts, thus reducing the impact of frosting ice on the image of the sample surface.

3. Results and discussion

3.1 Experimental results for macroscopic experiments

3.1.1 Inhibitory effect of the inhibitors. The kinetic inhibitory effects of PVP, PVCap, [BMP][BF_4], [BMP][BF_4] + PVP (1 : 1 mass ratio of [BMP][BF_4] to PVP) and [BMP][BF_4] + PVCap (1 : 1) on the formation of methane hydrate were experimentally investigated at 275.15 K and 6.95 MPa with two mass fractions of 1.0 and 2.0 wt%. The subcooling was about 8.0 K. The averaged induction time and statistical error was illustrated in Fig. 3. The phase equilibrium diagram of CH_4 hydrate was calculated by the CSMGem program.[1]

Seen from Fig. 3, the averaged induction time for each inhibitor system at 2.0 wt% was significantly longer than that at 1.0 wt%, while such an opposite trend happened to single PVCap. However, PVCap-containing mixed systems stilled exhibited stronger inhibition performance than other systems at the same concentrations of 1.0 and 2.0 wt%. According to the pressure change curve with time in Fig. 4, it was interestingly

 This journal is © The Royal Society of Chemistry 2020

Open Access Article. Published on 17 April 2020. Downloaded on 7/25/2025 1:18:10 AM.
This article is licensed under a Creative Commons Attribution-NonCommercial 3.0 Unported Licence.

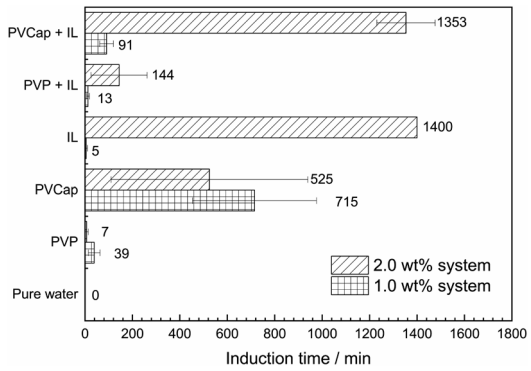

Fig. 3 Induction time of methane hydrate formation in different inhibitor systems.

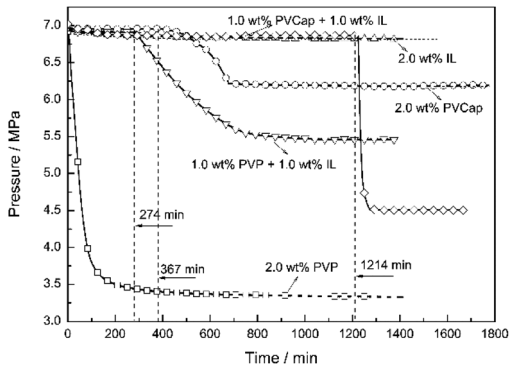

Fig. 4 Curves of pressures varying with time for methane hydrate formed in the presence of 2.0 wt% different inhibitor solutions at 275.15 K and 6.95 MPa.

found that there was almost no hydrate formed for the 2.0 wt% [BMP][BF_4] system, and the growth rate of gas hydrate was extremely low without sudden temperature rise or pressure drop. Due to the dissolution of methane gas in water agitated by the magnetic stirrer, the gas pressure initially decreased slightly. Noticeably, the value of pressure drop still achieved 0.16 MPa in the end. Although being undetectable from the pressure and temperature changes, small quantity of hydrate formed was still observed after opening the reactor, possibly because of very slow formation rate and quick removing reaction heat by water bath. Meanwhile, it was suggested that the [BMP][BF_4] may well hinder the growth rate of gas hydrate, but it was unable to effectively inhibit the hydrate nucleation.

3.1.2 The influence of subcooling on the performance of [BMP][BF_4]. The influence of subcooling on the performance of [BMP][BF_4] was further investigated. Three different subcooling conditions were operated under 6.95 MPa, 275.15 K and 6.95 MPa, 273.15 K and 12 MPa, 273.65 K namely, 8 K, 10 K and 15 K. The experimental results are illustrated in Fig. 5. The result shows that the [BMP][BF_4] system could not inhibit the hydrate nucleation rate. However, it was found that, even under high subcooling of 15 K, the [BMP][BF_4] system still effectively suppressed the growth rate of methane hydrate. As illustrated in Fig. 4, when the commercial kinetic inhibitors PVCap was

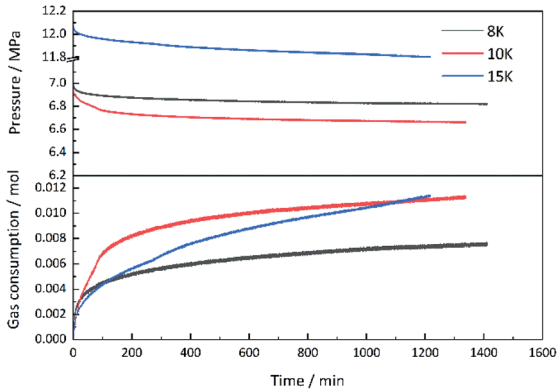

Fig. 5 Curves of pressure and gas consumption varying with time for methane hydrate formation with 2.0 wt% [BMP][BF_4] solution at different subcooling temperatures.

mixed with [BMP][BF_4], the induction time was up to 1214 min. The nucleation process was effectively inhibited.

As [BMP][BF_4] was hydrophilic and hygroscopic, it had strong electrostatic charges inducing interaction between ions and dipoles. Besides, BF_4^-, a representative hydrophilic group, helped [BMP][BF_4] to dissolve into water. The ions produced by [BMP][BF_4] in the solution might be adsorbed on some active nucleation sites, thereby reducing the number of available sites for hydrate nucleation and growth. In this way, the amount of gas, which could be consumed during this period, would decrease. An adsorption mechanism for inhibiting hydrate nucleation has been proposed in earlier study.[40–42] The hydrophilic carbonyl group in the 7-membered ring could enable PVCap to easily interact with water by forming hydrogen bonds, while the alkyl group in the backbone chain could interact with dissolved CH_4 gas through hydrophobic interaction.[43] Recently, Xu *et al.*[42] verified that PVCap prevented CH_4 hydrate nucleation and/or growth by adsorption onto the hydrate surface through molecular simulation. The unstable adsorption caused the hydrate destruction phenomenon and slowed down the hydrate growth. In addition, ILs might effectively penetrate deep into the space where the polymer chain was too large to reach, thereby hindering the hydrate formation. The result indicated a synergistic inhibitory effect by adding [BMF][BF_4] in PVCap. Since the mixture of [BMP][BF_4] and PVCap performed the best inhibitory effect, they were chosen for further investigation.

3.1.3 Effect of compound inhibitor concentration. The inhibition performance of [BMP][BF_4] + PVCap (1 : 1) at different concentrations on the formation of CH_4 hydrate was investigated. The changes in the pressure and temperature with the elapse of time at 273.65 K and 6.0 MPa (8.0 K subcooling) at 1.0 wt%, 1.5 wt% and 2.0 wt% mass concentrations were drawn in Fig. 6. The induction time for the 0.5 wt% [BMP][BF_4] + 0.5 wt% PVCap system was just about 86 min. For comparison, the systems of 0.75 wt% [BMP][BF_4] + 0.75 wt% PVCap and 1.0 wt% [BMP][BF_4] + 1.0 wt% PVCap prolonged the induction time up to 440 and 1290 min, respectively. This indicated that the inhibitory effect of the combined inhibitors was

Open Access Article. Published on 17 April 2020. Downloaded on 7/25/2025 1:18:10 AM.
This article is licensed under a Creative Commons Attribution-NonCommercial 3.0 Unported Licence.

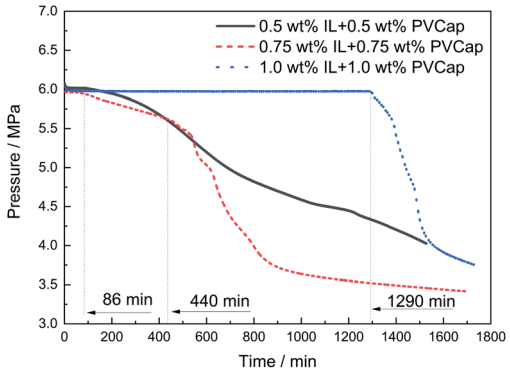

Fig. 6 Changes in pressure with elapse of time at different concentrations.

concentration dependent. As expected, the inhibitory effect increased with the increase of the concentration.[15,44]

3.1.4 Effect of compound inhibitor mass ratio. A series of experiments at 6.95 MPa and 275.15 K corresponding to 8.0 K subcooling were conducted to further explore the effect of different mass ratios of [BMP][BF_4] to PVCap on hydrate formation at the same concentration of 2.0 wt%. The inhibitory effect of the solution systems prepared by [BMP][BF_4] and PVCap at different ratios of 3 : 1, 2 : 1, 1 : 2 and 1 : 3 were investigated. At a low proportion of PVCap, the inhibition performance was almost negligible. The pressure dropped evidently at a very short induction time. Conversely, as shown in Fig. 7, the inhibitory effect of the compound inhibitor enhanced with the increase in the concentration of PVCap. From the perspective of induction time, the solution of compound inhibitor at 1 : 3 mass ratio of [BMP][BF_4] to PVCap exhibited an induction time of 103 min. The inhibitory effect of the compound inhibitor at 1 : 2 mass ratio of [BMP][BF_4] to PVCap was the best, and no hydrate formed during 1800 min. Solution of other ratios did not show significant induction time. From the perspective of pressure drop and CH_4 gas consumption rate, it was found that in the beginning each system showed similar pressure drop caused by the dissolution of CH_4 in aqueous solution. Subsequently, a solution with an increase in PVCap proportion could more remarkably suppress the methane gas consumption rate. When the ratio of [BMP][BF_4] to PVCap was 1 : 2, the gas consumption rate was almost zero. In summary, there was an optimal ratio 1 : 2 of [BMP][BF_4] to PVCap corresponding to the strongest inhibition performance of the mixture within our studied ratio range.

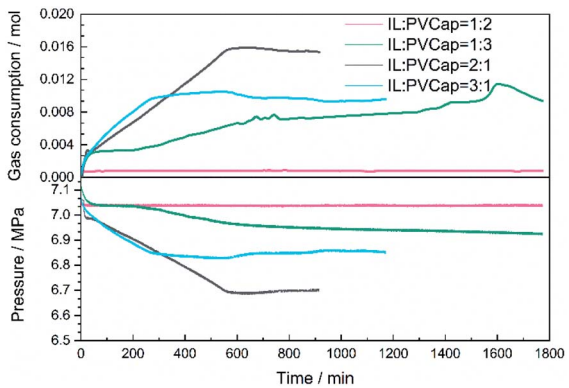

Fig. 7 Changes in pressure and gas consumption with elapse of time for methane hydrate formation in 2.0 wt% mixed systems of IL and PVCap at different mass ratios.

3.2 Microscopic experiment analyses

3.2.1 PXRD. PXRD was commonly used to determine the structure type of hydrate crystal. Fig. 8 illustrated the PXRD patterns of CH_4 hydrate samples formed in the presence of 2.0 wt% different inhibitor systems at 6.95 MPa and 275.15 K. For sI hydrate, the reflections for (320), (321) crystal planes were reported to be at approximately 27.0°, 28.0° 2θ, respectively.[39,45,46] Here, two typical crystal planes (320) and (321) of sI hydrate were observed at about 26.8° and 27.9° 2θ. The crystal planes (100), (002), (101) of Ih ice were observed at 22.7°, 24.1° and 25.6° 2θ, respectively. None diffraction peak of sII hydrate was observed (such as 20.7°and 29.2° 2θ corresponding to (400) and (440) crystal planes, respectively). The results confirmed that hydrate samples were pure sI hydrate. The peak intensity was sufficient, suggesting the high quality of samples. Moreover, compared with the PXRD spectrum of hydrate sample formed in pure water, it could be concluded that these inhibitors did not change the hydrate crystal structure.

3.2.2 Raman spectra. Fig. 9 compared the C–H region in the Raman spectra of CH_4 hydrates formed in the different inhibitor systems at 6.95 MPa and 275.15 K. According to "loose-cage-tight-cage model" of hydrate, two strong peaks at approximately 2903.4 cm^{-1} and 2913.5 cm^{-1} corresponded to the ν_1 C–H stretching vibration of CH_4 trapped into the large cages and small cages of the hydrate lattices, respectively. It was approximately 1–2 cm^{-1} lower than the previous data.[38,44,45] Despite of the difference possibly associated with the different temperatures, pressures and scanning range during the measurement, it was very close to the typical characteristics of sI CH_4 hydrate. Moreover, the Raman integrated peak intensity was known to be proportional to the concentration. Herein, the calculated ratio of the peak area of the former to the latter was nearly 3 : 1, indicating that the gas content in the large cages

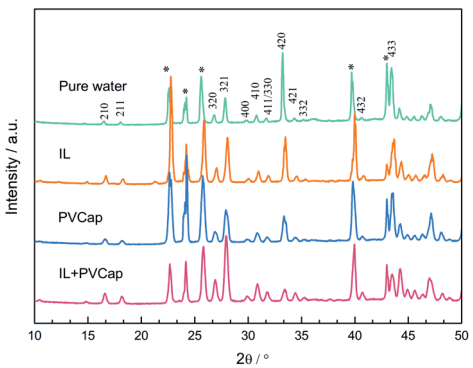

Fig. 8 PXRD patterns of hydrate formed in different systems.

This journal is © The Royal Society of Chemistry 2020

Open Access Article. Published on 17 April 2020. Downloaded on 7/25/2025 1:18:10 AM.
This article is licensed under a Creative Commons Attribution-NonCommercial 3.0 Unported Licence.

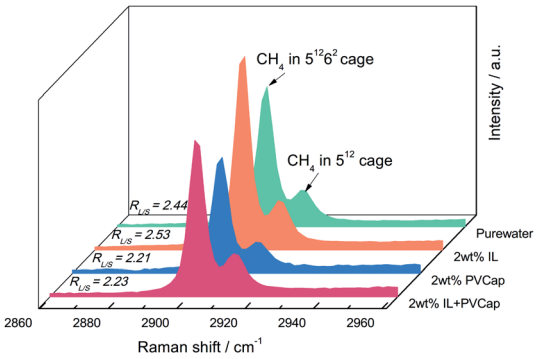

Fig. 9 Raman spectra of hydrate formed in different systems.

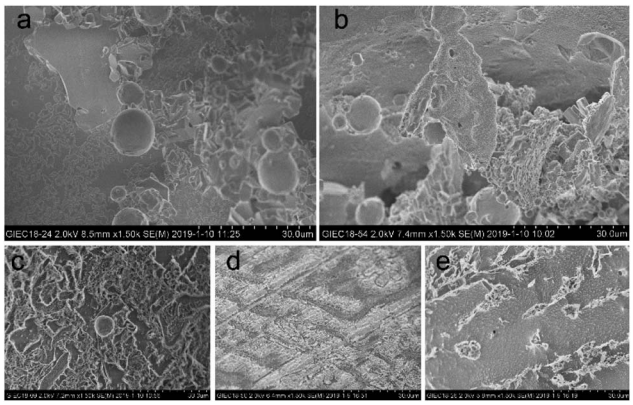

Fig. 10 SEM images of CH_4 hydrates formed in the presence of different solutions: (a) ice only; (b) pure water; (c) 2.0 wt% PVCap; (d) 2.0 wt% [BMP][BF_4]; (e) 2.0 wt% [BMP][BF_4] + PVCap (1 : 2).

was higher. The results confirmed the evidence from the PXRD analyses that the structure of the hydrate didn't change. The peak intensities had been used to reflect the gas occupancy in large and small cages.[47–49] Cage occupancy values by CH_4 and hydration number obtained in the presence of inhibitors from Raman spectra analyses were listed in Table 2.

Seen from Fig. 9, the relative ratios of large to small cage occupancies by CH_4 in the PVCap-containing systems were smaller than that in pure water except for single [BMP][BF_4] solution. This was because the presence of PVCap significantly reduced the absolute occupancy of methane molecules in the large cage, while [BMP][BF_4] played an opposite effect (see Table 2). The small cage occupancy was basically the same. It also directly led to the hydration number in [BMP][BF_4] system become the smallest.

For all the solution systems, the occupancy of methane molecules in the small cage was basically the same and higher than that in the large cage. This was because kinetic inhibitors interacted with water molecules or hydrate crystals to inhibit the formation or further growth of hydrate.[5,22] The small cages could form more easily, because a smaller number of water clusters was required than the large cages.[31] Combing the macroscopic kinetic experimental results with the Raman spectra analyses, it was found that [BMP][BF_4] at 2.0 wt% could continuously inhibit the growth of hydrates. However, their ability to inhibit the formation of large cages was weaker than PVCap. PVCap may inhibit the nucleation and growth process of hydrate for a period of induction time, and then lost its inhibitory effect. The results showed the different inhibition mechanisms of [BMP][BF_4] and PVCap, and further confirmed the results of the macroscopic experiment. When adding [BMP][BF_4] in PVCap, the influence of the mixture on the hydrate microstructure was very close to that of pure PVCap. This indicated that PVCap played a major role in the compound inhibitor and [BMP][BF_4] acted as a synergist in the presence of PVCap. The compound inhibitor could reduce the amount of PVCap without weakening its inhibitory performance.

3.2.3 Cryo-SEM. The morphology of hydrate sample powders was observed and photographed by cryo-SEM to further understand the influence of different inhibitors on the hydrate microstructure. As illustrated in Fig. 10, ice coexisted with gas hydrate. Initially, according to the morphology characteristics, it was difficult to discriminate gas hydrate from ice, because their surfaces were smooth and dense. After a short time (about 5 min), surface of gas hydrate became concave and porous, because of gas releasing from the decomposed hydrate and diffusion into ice under a vacuum condition. The analysis and photographing could be performed at this time. In addition, the appearance of pure ice was observed for comparison and supplement, as shown in Fig. 10(a). Zhang *et al.*,[50] discussed the microstructure of hydrate with the additive of KHIs (PVCap and PVCSCOOH). They found an obvious trend that the higher the PVCap concentration, the more chaotic and porous the hydrate surface. Similarly, the surface of hydrate in Fig. 10(c) was more chaotic than that of pure water system. However, for 2.0 wt% [BMP][BF_4] system, the opposite phenomenon was found in Fig. 10(d). The neat square arrangement could be clearly distinguished. Although the hydrate was no longer smooth and flat, it clearly showed a regular arrangement. This indicated the distinct effect of single [BMP][BF_4] and PVCap on the hydrate morphology. An

Table 2 Cage occupancy values obtained in the presence of inhibitors

Inhibitor systems	Concentration (wt%)	Small cage occupancy, Θ_S	Large cage occupancy, Θ_L	Hydration number
Pure water (control group)	—	0.9997	0.81209	6.6939
[BMP][BF_4] (IL)	2.0	0.99951	0.84141	6.5272
PVCap	2.0	0.99989	0.73733	7.1609
IL + PVCap	2.0	0.99988	0.74374	7.1183

Open Access Article. Published on 17 April 2020. Downloaded on 7/25/2025 1:18:10 AM.
This article is licensed under a Creative Commons Attribution-NonCommercial 3.0 Unported Licence.

interesting phenomenon was that the hydrate samples, formed in the 2.0 wt% [BMP][BF_4] + PVCap (1 : 2) system, exhibited both disorder and order as seen in Fig. 10(e). On the one hand, most of the hydrate surfaces became smooth and dense like that of pure water system. On the other hand, many cylindrical hydrates protruded on the surface, causing the hydrate surface to become rough.

4. Conclusion

In this work, the inhibitory effect of single [BMP][BF_4] and commercial kinetic inhibitor PVCap as well as their mixture on methane hydrate formation was investigated. The kinetic experimental data obtained in a high pressure reactor showed that [BMP][BF_4] could significantly inhibit the growth rate of hydrate, but was unable to delay the hydrate nucleation when used alone. Then, the inhibition performance of the compound inhibitors of [BMP][BF_4] with PVCap was tested at different concentrations and mass ratios. [BMP][BF_4] was found to exhibit excellent synergistic effect in the presence of PVCap on CH_4 hydrate. When the mixed inhibitor concentration was 2.0 wt% at a mass ratio 1 : 2 of [BMP][BF_4] to PVCap, the best inhibitory effect was obtained. Microscopic results measured by PXRD and Raman spectrometers revealed that each inhibitor system had no obvious effect on the crystal structure of methane hydrate. Cryo-SEM images indicated that [BMP][BF_4] and PVCap systems had distinct effect on the morphology of hydrate. Furthermore, similar to other studies, such as in dye-sensitized solar cells,[51] energy storage,[52] biomass energy,[53] sodium-ion batteries,[54] sensors,[55] *etc*, it is necessary to perform a multivariate study in order to obtain the optimum conditions in future work, taking into account all the relevant variables and their interactions and exploring the internal law to strengthen inhibitory ability.

Conflicts of interest

There are no conflicts to declare.

Acknowledgements

This work was supported by the National Natural Science Foundation of China (No. 51506202), project of Guangzhou Science and Technology-Pearl River S&T Nova Program of Guangzhou (No. 201806010114), and National Key Research and Development Plan of China (No. 2016YFC0304002).

References

1 E. D. Sloan Jr and C. A. Koh, *Clathrate Hydrates of Natural Gases*, CRC Press, 2007.
2 C. Gutt, B. Asmussen, W. Press, M. R. Johnson, Y. P. Handa and J. S. Tse, *J. Chem. Phys.*, 2000, **113**, 4713–4721.
3 E. D. Sloan, *Nature*, 2003, **426**, 353–359.
4 T. Kuznetsova, A. Sapronova, B. Kvamme, K. Johannsen and J. Haug, in *Macromolecular Symposia*, Wiley Online Library, 2010, vol. 287, pp. 168–176.
5 M. A. Kelland, *Energy Fuels*, 2006, **20**, 825–847.
6 Y. h. Sohn, J. Kim, K. Shin, D. Chang, Y. Seo, Z. M. Aman and E. F. May, *Chem. Eng. Sci.*, 2015, **126**, 711–718.
7 J. D. Lee and P. Englezos, *Chem. Eng. Sci.*, 2005, **60**, 5323–5330.
8 A. K. Sum, C. A. Koh and E. D. Sloan, *Ind. Eng. Chem. Res.*, 2009, **48**, 7457–7465.
9 C. B. Bavoh, B. Partoon, B. Lal and L. Kok Keong, *J. Nat. Gas Sci. Eng.*, 2017, **37**, 425–434.
10 L. U. Udegbunam, J. R. DuQuesnay, L. Osorio, V. K. Walker and J. G. Beltran, *J. Chem. Thermodyn.*, 2018, **117**, 155–163.
11 C. B. Bavoh, O. Nashed, M. S. Khan, B. Partoon, B. Lal and A. M. Sharif, *J. Chem. Thermodyn.*, 2018, **117**, 48–53.
12 J. H. Yang and B. Tohidi, *Chem. Eng. Sci.*, 2011, **66**, 278–283.
13 V. Thieu and L. M. Frostman, in *Proceedings – SPE International Symposium on Oilfield Chemistry*, Society of Petroleum Engineers, 2005, pp. 703–709.
14 P. C. Chua and M. A. Kelland, *Energy Fuels*, 2018, **32**, 1674–1684.
15 Z. Long, Y. He, X. B. Zhou, D. L. Li and D. Q. Liang, *Fluid Phase Equilib.*, 2017, **439**, 1–8.
16 M. R. Talaghat, *J. Nat. Gas Sci. Eng.*, 2014, **19**, 215–220.
17 W. Ke, T. M. Svartaas and H. K. Abay, in *ICGH 2011*, 2011, vol. 324, pp. 17–21.
18 B. J. Anderson, J. W. Tester, G. P. Borghi and B. L. Trout, *J. Am. Chem. Soc.*, 2005, **127**, 17852–17862.
19 W. Ke and M. A. Kelland, *Energy Fuels*, 2016, **30**, 10015–10028.
20 D. Lovell, C. Canada and M. Pakulski, in *SPE Proceedings – Gas Technology Symposium*, Society of Petroleum Engineers, 2002, pp. 309–315.
21 A. Perrin, O. M. Musa and J. W. Steed, *Chem. Soc. Rev.*, 2013, **42**, 1996–2015.
22 M. A. Kelland, F. Gausland and K. Tsunashima, *Chem. Eng. Sci.*, 2013, **98**, 12–16.
23 J. Hu, S. J. Li, Y. H. Wang, X. M. Lang, Q. P. Li and S. S. Fan, *J. Nat. Gas Chem.*, 2012, **21**, 126–131.
24 P. C. Chua and M. A. Kelland, *Energy Fuels*, 2013, **27**, 1285–1292.
25 C. W. Xiao and H. Adidharma, *Chem. Eng. Sci.*, 2009, **64**, 1522–1527.
26 K. N. Marsh, A. Deev, A. C. T. Wu, E. Tran and A. Klamt, *Korean J. Chem. Eng.*, 2002, **19**, 357–362.
27 J. P. Hallett and T. Welton, *Chem. Rev.*, 2011, **111**, 3508–3576.
28 C. W. Xiao, N. Wibisono and H. Adidharma, *Chem. Eng. Sci.*, 2010, **65**, 3080–3087.
29 B. Partoon, N. M. S. Wong, K. M. Sabil, K. Nasrifar and M. R. Ahmad, *Fluid Phase Equilib.*, 2013, **337**, 26–31.
30 X. D. Shen, X. B. Zhou and D. Q. Liang, *Energy Fuels*, 2019, **33**, 1422–1432.
31 S. P. Kang, T. Jung and J. W. Lee, *Chem. Eng. Sci.*, 2016, **143**, 270–275.
32 J. W. Lee, J. Y. Shin, K. S. Kim and S. P. Kang, *Energy Fuels*, 2016, **30**, 9162–9169.
33 J. W. Lee, J. Y. Shin, K. S. Kim and S. P. Kang, *Energy Fuels*, 2016, **30**, 3879–3885.

 This journal is © The Royal Society of Chemistry 2020

Open Access Article. Published on 17 April 2020. Downloaded on 7/25/2025 1:18:10 AM.
This article is licensed under a Creative Commons Attribution-NonCommercial 3.0 Unported Licence.

34 M. Tariq, D. Rooney, E. Othman, S. Aparicio, M. Atilhan and M. Khraisheh, *Ind. Eng. Chem. Res.*, 2014, **53**, 17855–17868.
35 X. D. Shen, L. L. Shi, Z. Long, X. B. Zhou and D. Q. Liang, *J. Mol. Liq.*, 2016, **223**, 672–677.
36 C. Coquelet, A. Chapoy and D. Richon, *Int. J. Thermophys.*, 2004, **25**, 133–158.
37 D. Y. Peng and D. B. Robinson, *Ind. Eng. Chem. Fundam.*, 1976, **15**, 59–64.
38 S. Y. Hong, J. Il Lim, J. H. Kim and J. D. Lee, *Energy Fuels*, 2012, **26**, 7045–7050.
39 X. B. Zhou, Z. Long, S. Liang, Y. He, L. Z. Yi, D. L. Li and D. Q. Liang, *Energy Fuels*, 2016, **30**, 1279–1286.
40 L. Jensen, K. Thomsen and N. von Solms, *Chem. Eng. Sci.*, 2008, **63**, 3069–3080.
41 L. Jensen, H. Ramloøv, K. Thomsen and N. Von Solms, *Ind. Eng. Chem. Res.*, 2010, **49**, 1486–1492.
42 J. F. Xu, L. W. Li, J. X. Liu, X. P. Wang, Y. G. Yan and J. Zhang, *Phys. Chem. Chem. Phys.*, 2018, **20**, 8326–8332.
43 S. P. Kang, E. S. Kim, J. Y. Shin, H. T. Kim, J. W. Kang, J. H. Cha and K. S. Kim, *RSC Adv.*, 2013, **3**, 19920–19923.
44 Z. Long, X. B. Zhou, D. Q. Liang and D. L. Li, *J. Chem. Eng. Data*, 2015, **60**, 2728–2732.
45 J. M. Schicks, M. Luzi and B. Beeskow-Strauch, *J. Phys. Chem. A*, 2011, **115**, 13324–13331.
46 S. Takeya and J. A. Ripmeester, *ChemPhysChem*, 2010, **11**, 70–73.
47 J. A. Ripmeester and C. I. Ratcliffe, *J. Phys. Chem.*, 1988, **92**, 337–339.
48 J. H. van der Waals and J. C. Platteeuw, *Adv. Chem. Phys.*, 2007, 1–57.
49 H. L. Lu, I. Moudrakovski, M. Riedel, G. Spence, R. Dutrisac, J. Ripmeester, F. Wright and S. Dallimore, *J. Geophys. Res.: Solid Earth*, 2005, **110**, 1–9.
50 Q. Zhang, X. D. Shen, X. B. Zhou and D. Q. Liang, *Energy Fuels*, 2017, **31**, 839–846.
51 F. Bella, M. Imperiyka and A. Ahmad, *J. Photochem. Photobiol., A*, 2014, **289**, 73–80.
52 D. L. Cao, G. Hong and A. T. Le, *J. Energy Storage*, 2020, **28**, 101311.
53 A. Narani, P. Coffman, J. Gardner, C. Li, A. E. Ray, D. S. Hartley, A. Stettler, N. V. S. N. M. Konda, B. Simmons, T. R. Pray and D. Tanjore, *Bioresour. Technol.*, 2017, **243**, 676–685.
54 F. Bella, A. B. Muñoz-García, F. Colò, G. Meligrana, A. Lamberti, M. Destro, M. Pavone and C. Gerbaldi, *ACS Omega*, 2018, **3**, 8440–8450.
55 B. Miccoli, V. Cauda, A. Bonanno, A. Sanginario, K. Bejtka, F. Bella, M. Fontana and D. Demarchi, *Sci. Rep.*, 2016, **6**, 29763.